

## Article

# Highly Fluorescent Carbon Dots as a Potential Fluorescence Probe for Selective Sensing of Ferric Ions in Aqueous Solution

Raji Atchudan <sup>1,\*</sup>, Somasundaram Chandra Kishore <sup>2,†</sup>, Thomas Nesakumar Jebakumar Immanuel Edison <sup>1,†</sup>, Suguna Perumal <sup>1,†</sup>, Rajangam Vinodh <sup>3,†</sup>, Ashok K. Sundramoorthy <sup>4,†</sup>, Rajendran Suresh Babu <sup>5,†</sup>, Muthulakshmi Alagan <sup>6,†</sup> and Yong Rok Lee <sup>1,\*</sup>

<sup>1</sup> School of Chemical Engineering, Yeungnam University, Gyeongsan 38541, Korea; jebakumar84@yu.ac.kr (T.N.J.I.E.); suguna.perumal@gmail.com (S.P.)

<sup>2</sup> Department of Biomedical Engineering, Saveetha School of Engineering, Saveetha Institute of Medical and Technical Sciences, Saveetha University, Chennai 602105, India; schandrakishore30@gmail.com

<sup>3</sup> School of Electrical and Computer Engineering, Pusan National University, Busan 46241, Korea; vinoth6482@gmail.com

<sup>4</sup> Department of Chemistry, SRM Institute of Science and Technology, Kattankulathur 603203, India; ashokkus@srmist.edu.in

<sup>5</sup> Laboratory of Experimental and Applied Physics, Centro Federal de Educação Tecnológica Celso Suckow da Fonseca (CEFET/RJ), Av. Maracanã 229, Rio de Janeiro 20271-110, Brazil; ryesbabu@gmail.com

<sup>6</sup> Faculty of Information and Communication Science, University of Information Science and Technology “St. Paul the Apostle”, 787487 Ohrid, North Macedonia; almuthulakshmi@gmail.com

\* Correspondence: atchudanr@yu.ac.kr (R.A.); yrlee@yu.ac.kr (Y.R.L.)

† Authors contributed equally to this work.



**Citation:** Atchudan, R.; Kishore, S.C.; Edison, T.N.J.I.; Perumal, S.; Vinodh, R.; Sundramoorthy, A.K.; Babu, R.S.; Alagan, M.; Lee, Y.R. Highly Fluorescent Carbon Dots as a Potential Fluorescence Probe for Selective Sensing of Ferric Ions in Aqueous Solution. *Chemosensors* **2021**, *9*, 301. <https://doi.org/10.3390/chemosensors9110301>

Academic Editor: Camelia Bala

Received: 30 September 2021

Accepted: 22 October 2021

Published: 25 October 2021

**Publisher's Note:** MDPI stays neutral with regard to jurisdictional claims in published maps and institutional affiliations.



**Copyright:** © 2021 by the authors. Licensee MDPI, Basel, Switzerland. This article is an open access article distributed under the terms and conditions of the Creative Commons Attribution (CC BY) license (<https://creativecommons.org/licenses/by/4.0/>).

**Abstract:** This paper's emphasis is on the development of a fluorescent chemosensor for Fe<sup>3+</sup> ions in an aqueous solution, using hydrophilic carbon dots (O-CDs). A simple, cost-effective, and environmentally friendly one-step hydrothermal synthesis method was used to synthesize fluorescent hydrophilic O-CDs from *Oxalis corniculata* (Family; Oxalidaceae). The graphitic structure and size distribution of the O-CDs was verified by X-ray diffraction, Raman spectroscopy, and high-resolution transmission electron microscopy studies. The resulting O-CDs had a near-spherical shape and an adequate degree of graphitization at the core, with an average diameter of 4.5 nm. X-ray photoelectron and Fourier transform infrared spectroscopy methods revealed the presence of several hydrophilic groups (carbonyl, amine, carboxyl, and hydroxyl, along with nitrogen and oxygen-rich molecules) on the surface of O-CDs. The synthesized hydrophilic O-CDs with excitation wavelength-dependent emission fluorescence characteristics showed a high quantum yield of about 20%. Besides this, the hydrophilic O-CDs exhibited a bright and controllable fluorescence with prolonged stability and photo-stability. These fluorescent hydrophilic O-CDs were used as a nanoprobe for the fluorometric identification of Fe<sup>3+</sup> ions in an aqueous solution, with high sensitivity and selectivity. By quenching the blue emission fluorescence of this nanosensor, a highly sensitive Fe<sup>3+</sup> ion in the range of 10–50 μM with a minimum detection limit of 0.73 μM was achieved. In addition, the developed nanosensor can be used to sense intracellular Fe<sup>3+</sup> ions with high biocompatibility and cellular imaging capacity, and it has a lot of potential in biomedical applications.

**Keywords:** *Oxalis corniculata*; hydrothermal; hydrophilic carbon dots; fluorescent sensor; fluorescence quenching

## 1. Introduction

Heavy metal ions are one of the most dangerous contaminants that have been continuously released into the environment by industrial and other human activities, posing serious health and environmental risks [1,2]. In particular, the ferric (Fe<sup>3+</sup>) ion is an essential transition metal ion that is one of the most harmful and pervasive contaminants in aquatic systems, and is now a primary source of concern [3,4]. In the human body, Fe<sup>3+</sup>

ions are one of the most abundant metal ions involved in cellular metabolism, enzyme catalysis, oxygen transport, and deoxyribonucleic acid and ribonucleic acid synthesis, as well as many other physiological and pathological activities [5]. Excess or deficiency of iron can lead to serious complications such as anemia [6], cognitive loss [7], liver damage [8], heart failure [9], diabetes [10], renal failure [11], and even death. Consequently, specific  $\text{Fe}^{3+}$  ion concentration detection in environmental and biological materials is extremely important and has become a hot subject among researchers.

In this context, developing appropriate and effective techniques for detection, quantification and rapid determination of  $\text{Fe}^{3+}$  ions with high sensitivity and selectivity are considered very critical for human health and environmental observation. Many conventional methods, such as electrochemical sensors [12], atomic absorption spectroscopy [13], polarography [14], and plasma mass spectrometry [15], have been developed for the detection of metal ions, but they all have inherent flaws that limit their clinical relevance—such as the need for complex equipment and time-consuming sample preparation.

Fluorescent probes well-known tool for the detection of metal ions have attracted a lot of attention recently because of their extreme accuracy, sensitivity, speed of analysis, and easy operation [16–20]. Several fluorescent probes, such as fluorescent organic dyes [21], metal nanoparticles [22], and semiconductor quantum dots [23], have been used to date as remarkable examples of these uses. Nevertheless, these nanomaterials have certain pitfalls, such as rapid oxidation, photobleaching of the fluorescent dye, potential toxicity, and limited photo-response, which restrict their extensive application and production. Exploration of new, highly fluorescent green quantum dots or similar nanomaterials with strong photostability and excellent biocompatibility is indeed critical. Fluorescence (FL) quenching efficacy is, then, one of the most successful strategies for metal ion detection [24,25].

Carbon dots (CDs) have recently gained the interest of researchers as potential bioimaging labels and sensors due to their remarkable properties, which include brilliant FL, great photo-stability, adjustable FL emission, excellent biocompatibility, minimal toxicity, and superior water dispersibility/solubility [18,26–30]. Detection of ions such as  $\text{Fe}^{3+}$ ,  $\text{Hg}^{2+}$ ,  $\text{Cu}^{2+}$ ,  $\text{Zn}^{2+}$ , Cr (IV),  $\text{Ag}^{2+}$ ,  $\text{As}^{3+}$ , and  $\text{Eu}^{3+}$ ; and sensing of organics such as insecticides, glutathione, methimazole, picric acid, nitro-compounds,  $\alpha$ -glucosidase, and cholesterol chitosan have all been shown using CDs [31–33]. For this purpose, green CD synthesis has gotten a lot of interest, since it makes work easier, saves time and resources, and creates long-lasting environmentally friendly material with a high quantum yield [34]. Biological sources containing C, O, and H components contain carbohydrate benefaction in the synthesis of CDs with rich surface functional groups. Additionally, CDs' surface functional groups linked to oxygen can improve water solubility and FL characteristics necessary for fluorescent probes [35]. Heteroatom doping of CDs also enhances FL efficiency as well as providing active sites in the CDs, allowing for a wider range of applications in analysis and sensing [36]. Natural biomass such as *Phyllanthus acidus* fruits [18], banana peel [37], *Prunus avium* fruit extract [38], *Chionanthus retusus* fruits [24], betel leaf [39], and peach fruits [40] are just a few examples of the precursors of carbon nanodots investigated by our research group.

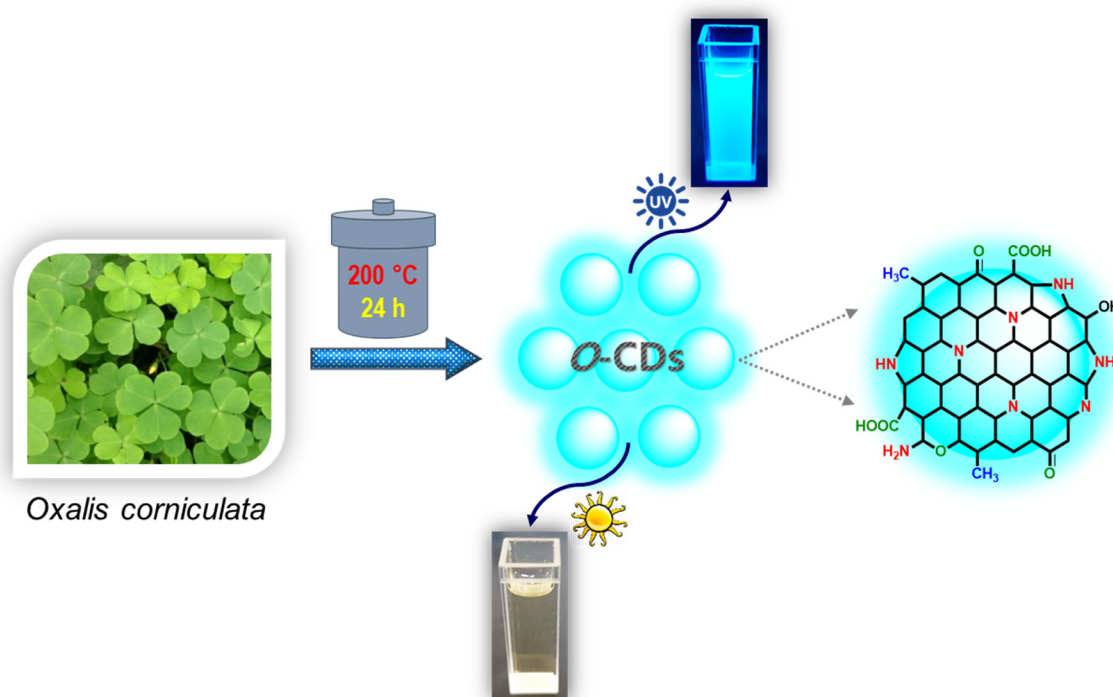
Although using natural carbon precursors to synthesize CDs is a viable option, finding a novel natural carbon precursor with acceptable physicochemical and optical characteristics remains a challenge. It would also be ideal if an easy and inexpensive precursor for synthesizing CDs could be developed. *Oxalis corniculata* is an herbaceous plant originating from India, mainly used for traditional medical treatment for various ailments such as liver problems, stomach pain, dysentery, and diarrhea. The plant extract mainly encompasses proteins, alkaloids, carbohydrates, saponins, phenols, flavonoids, and tannins [41]. In this present investigation, we produced a very efficient fluorescent probe for label-free selective and sensitive detection of  $\text{Fe}^{3+}$  ions with a limit of detection as minimal as 0.73  $\mu\text{M}$ , using an incredibly easy and green hydrothermal treatment of *Oxalis corniculata* leaf extract to produce hydrophilic CDs with blue emission and significant quantum yield. The synthesized *Oxalis corniculata*-derived carbon dots (O-CDs) with proven excitation-emission dependent

FL characteristics will be potential candidates as fluorescent probes for detecting  $\text{Fe}^{3+}$  ions in water with high sensitivity and selectivity.

## 2. Experimental

### Preparation of O-CDs

The synthesis process is demonstrated in Scheme 1. The leaves of *Oxalis corniculata* were properly cleaned in de-ionized water before being crushed. Cotton was used to filter the smashed extract, which was then followed by Whatman filter paper. The filtered plant extract was placed into a Teflon-lined stainless-steel autoclave with a capacity of 50 mL, for the production of O-CDs. The autoclave was properly sealed before being heated to 200 °C for 24 h. The autoclave was cooled to room temperature after the process. The dark brown solution obtained was centrifuged, the precipitate was removed, and the liquid in the supernatant was analyzed.



**Scheme 1.** Graphic for the synthesis of hydrophilic O-CDs from *Oxalis corniculata* by simple hydrothermal method.

## 3. Results and Discussion

### 3.1. Structural and Optical Properties of the Hydrophilic O-CDs

The surface morphology of the synthesized hydrophilic O-CDs was examined with FESEM. Figure S1 and Figure 1 illustrate the micrographs of hydrophilic O-CDs with their elemental mapping. From the micrographs in Figure 1a and Figure S1a–d, the O-CDs are observed to be arranged in an agglomerated fashion. The O-CDs with hygroscopic properties when placed over the silicon wafer for examination get adhered together after drying. This phenomenon could be ascribed to the presence of certain functional groups present on the surface and edges of O-CDs. In addition, the presence of dangling bonds on the surface of O-CDs could also promote this wrinkle type of formation on the silicon substrate. Figure 1b–d depicts the elemental mapping of various constituents present over the surface of O-CDs. The images highlighted with green, yellow, and red colors represent the presence of carbon, nitrogen, and oxygen elements present on O-CDs, respectively. All these elements were found to be uniformly dispersed; among them, carbon was observed to be dominating the other elements with regards to quantity. The combined elemental mapping of C, O, and N is observed from Figure 1e, showing the uniform distribution of

these elements with smaller particle sizes. The EDS spectrum shown in Figure 1f further illustrates the presence of energy peaks representing the C, N, and O in *O*-CDs. The morphology of the synthesized hydrophilic *O*-CDs was further analyzed with the aid of TEM and HRTEM images. Figure 2a,b clearly show the homogeneous dispersion of fine particles, with particle size varying in the range 3–7 nm, with an average particle size of 4.5 nm (inset of Figure 2b). The HRTEM images shown in Figure 2c,d show nearly spherical-shaped particles possessing a crystalline inner core surrounded by the amorphous layered surface. The surface amorphous type layer could be due to the presence of defects or any functional group attached over the *O*-CDs. The inner core of the *O*-CDs shows lattice fringes with an interplanar spacing distance of 0.21 nm, confirming the existence of a crystalline carbon core.

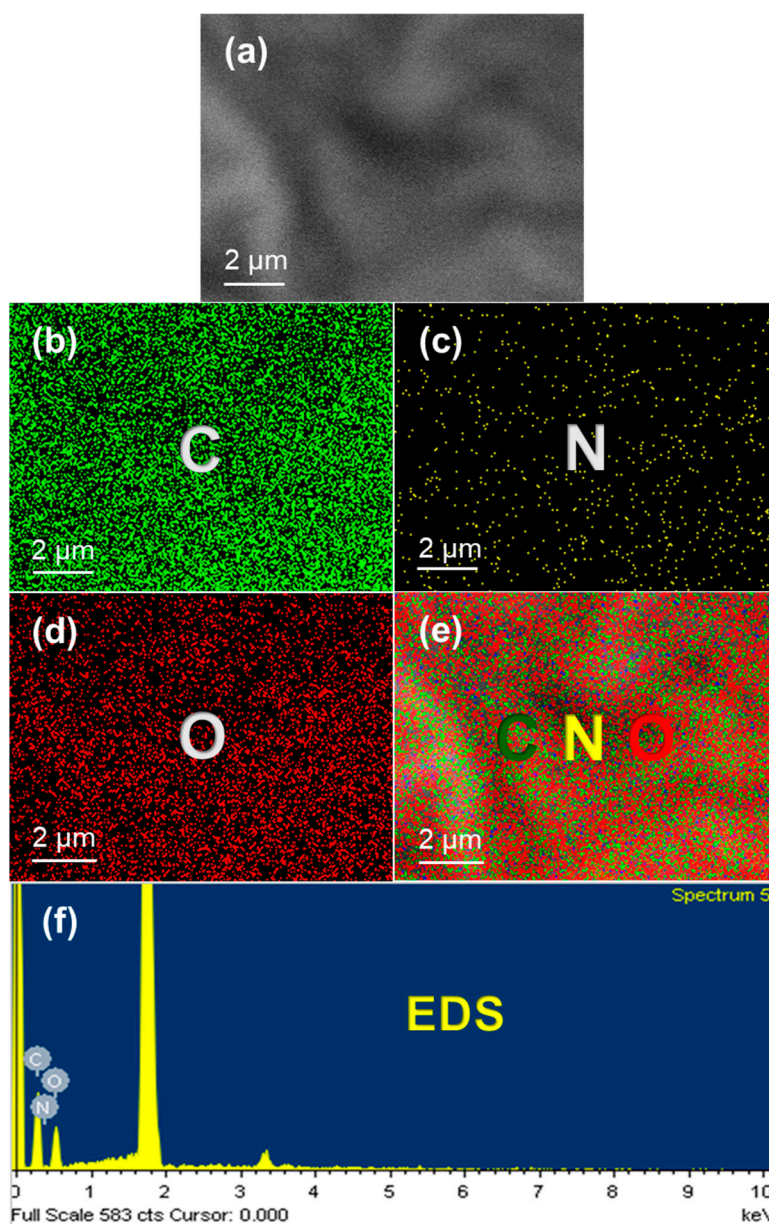


**Figure 1.** (a) FESEM image (mapping area), and the corresponding carbon (b), nitrogen (c), oxygen (d), and overlap (e) elemental mapping of synthesized hydrophilic *O*-CDs. (f) The EDS graph of synthesized hydrophilic *O*-CDs.

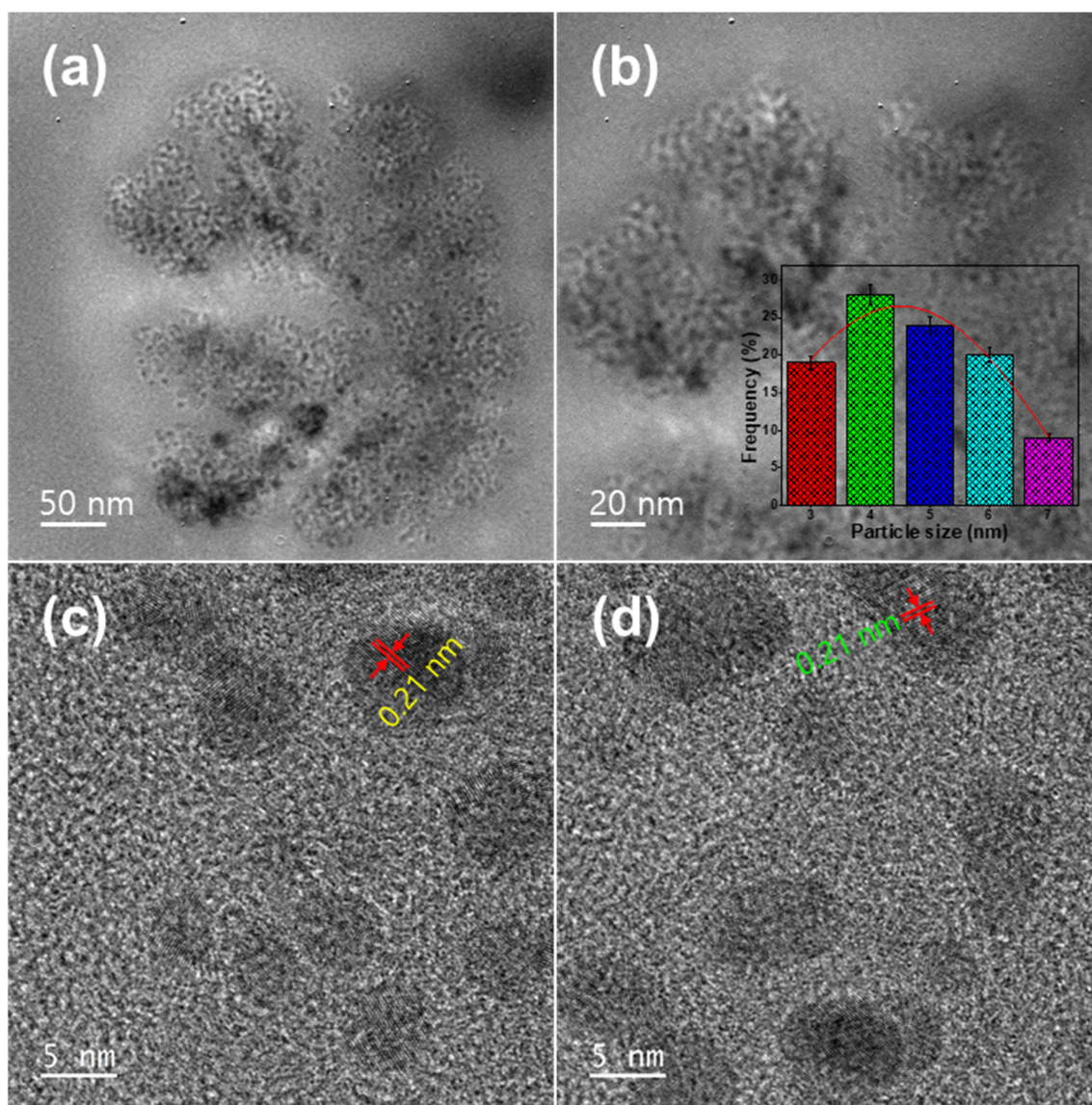


**Figure 2.** (a,b) TEM images and (inset b) the corresponding particle size distribution graph of the synthesized hydrophilic O-CDs. (c,d) HRTEM images with lattice fringes of synthesized hydrophilic O-CDs.

The phase purity, crystallinity, and graphitization nature of O-CDs were assessed using XRD and Raman spectroscopy studies. Figure S2a shows the XRD pattern of as-synthesized O-CDs. The pattern indicates the presence of two relevant peaks around at ( $2\theta =$ ) 23 and 43°, representing the (002) and (100) planes, respectively—authenticating the presence of carbon [42,43]. This observation well coincides with the HRTEM observation for the formation of crystalline carbon at the core of O-CDs. The d-spacing value calculated from the Bragg equation for the (100) and (002) planes was found to be 0.21 and 0.39 nm, respectively—which is consistent with the HRTEM results. It is interesting to note that the d-spacing of 0.39 nm was greater than the conventional bulk graphite value (0.34 nm). Presumably, this variation in d-space value could account for the formation of amorphous coating over the edges or surface of O-CDs, perhaps generated by various moieties during the synthesis process. In addition, the XRD peak at (002) displayed a broad area, indicating O-CD particles at nano size or with an amorphous nature [17]. This finding supports the development of both amorphous and crystalline carbon at the surface and core of O-CDs, respectively. The Raman spectrum of the O-CDs was obtained as shown in Figure S2b. The spectrum shows two dominant peaks at 1360 and 1590  $\text{cm}^{-1}$ , representing the D-

band and G-band of carbon, respectively [33]. These bands indicate the  $sp^3$  (D-band) and  $sp^2$  (G-band) configuration of carbon atoms placed in the O-CDs due to disordered and graphitic carbon, respectively. These peaks were observed to be merged with each other. The intensity ratio of these peaks ( $I_D/I_G$ ) was calculated to be 0.65 ( $I_D/I_G < 1$ ); indicating moderate graphitization due to the presence of more functional groups or amorphous carbon over the O-CDs [37]. This observation also agrees well with the findings obtained in HRTEM and XRD that O-CDs consist of functional groups with moderate graphitization and excellent purity.

To study the presence of functional groups and the elemental composition of O-CDs, ATR-FTIR and XPS analyses were performed. Figure S3 demonstrates the ATR-FTIR spectrum of as-synthesized O-CDs. The spectrum shows a broad absorption band at 3150–3450  $cm^{-1}$ , attributed to a stretching band of N–H/O–H [44]; and at 2955 and 2856  $cm^{-1}$ , indicating asymmetric and symmetric C–H functional groups present over the O-CDs [45]. The functional groups, such as C–OH and C–O–C, were confirmed by absorption band formation at 1295 and 1050–1100  $cm^{-1}$ , respectively. The peaks positioned at 1665, 1575, and 1455  $cm^{-1}$  reveal the occurrence of C=O, C=C, C–N bonding, respectively [18]. The absorption band corresponding to C=C signifies the  $sp^2$  hybridized carbon formed by the carbonization process through the hydrothermal method. Moreover, the out plane of the  $-CH_2$  group in aromatic carbon is revealed from the peak obtained between 570 and 700  $cm^{-1}$ . Thus, it is well confirmed that the O-CDs consist of various functional groups such as carbonyl, amine, carboxyl, and hydroxyl, along with nitrogen and oxygen-rich molecules without any impurities. This observation well matches with the XRD, HRTEM, and Raman spectroscopy findings, confirming the presence of several functional groups on O-CDs. As a result, these observations suggest that the presence of these functional groups inhibits the hydrophilic functionality of the O-CDs, thereby making them dispersible/soluble in the aqueous medium and suitable for potential application in chemosensors.

For a deeper understanding of elemental composition and atomic bonding, the XPS spectrum was analyzed and shown in Figure 3. The XPS survey spectrum illustrated in Figure 3a shows the formation of three major peaks centered at 284, 400, and 532 eV—representing the existence of C (1s), N (1s), and O (1s) elements, respectively, on O-CDs without any presence of impurities. Moreover, the high-resolution XPS peaks obtained for C (1s) in Figure 3b can be deconvoluted into four distinct binding energy (BE) peaks. The peaks obtained at 284.8, 285.9, 286.9, and 288.5 eV were ascribed to C=C/C–C, C–O/C–N, C=O/C=N, and O=C–OH bonding, respectively [33]. Noteworthy, the C=C/C–C bonding predominantly signified the  $sp^2$  carbon present in O-CDs. Figure 3c shows the Gaussian fitting of three deconvoluted peaks related to N (1s), with BE values at 399.0, 400.0, and 401.3 eV, signifying the bonding of nitrogen in C–N–C (pyridinic-N), C–N–H (pyrrolic-N), and (C<sub>3</sub>)–N (graphitic-N) forms, respectively [18]. The nature of bonding of oxygen in O-CDs was analyzed using the high-resolution spectrum of O (1s), as shown in Figure 3d. The three deconvoluted peaks of O (1s) at BEs 531.3, 532.4, and 533.3 eV correspond to C=O, C–O/C–OH, and O=C–OH bonding, respectively [18]. The presence of oxygen- and nitrogen-containing groups on the O-CDs' surface is yet again proved by this analysis, in addition to ATR-FTIR assessment. These oxygen-containing functional groups would make O-CDs more disseminated and dispersible/soluble in an aqueous environment, allowing them to be utilized in a variety of biological applications.

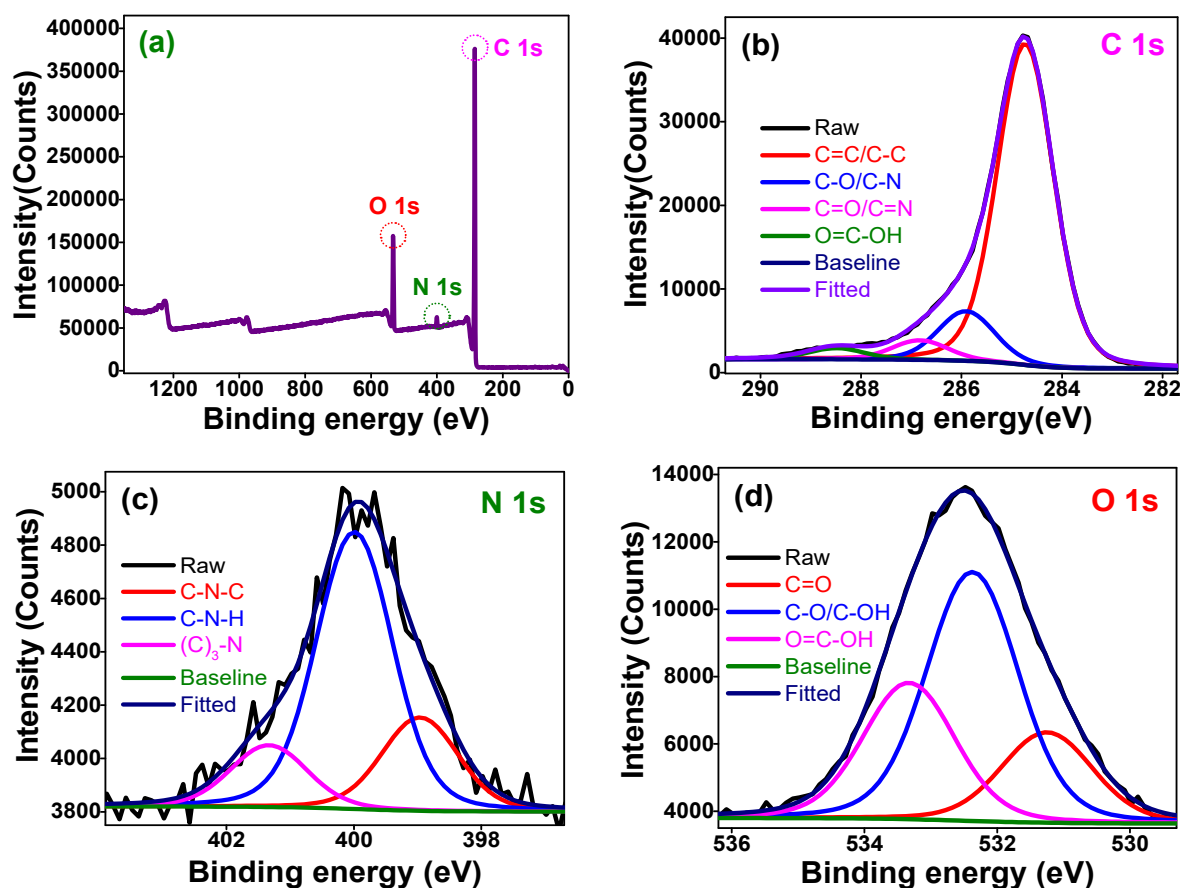


**Figure 3.** (a) XPS survey spectrum and the corresponding high-resolution C 1s (b), N 1s (c), and O 1s (d) spectra of the synthesized hydrophilic O-CDs.

The optical properties of hydrophilic O-CDs were examined with UV-visible (UV-vis) absorbance and FL spectroscopy at room temperature. Figure 4a depicts the UV-vis absorbance band with three broad peaks; where  $n \rightarrow \pi^*$  transition of  $sp^3$  hybrid orbitals present in C=O and C=N is substantiated by 317 nm and  $\pi \rightarrow \pi^*$  transition of  $sp^2$  hybrid orbitals (C=C) by bands in the range 249–274 nm [18]. The fluorescent emission of O-CDs under UV light irradiation is ensured by such a broad absorption band. In carbon nanoparticles, the phenomenon of emission wavelength dependency on excitation wavelength is a typical occurrence. The inset of Figure 4a shows the formation of brilliant blue FL when a UV light ( $\lambda = 365$  nm) is exposed to the O-CDs, whereas no light is emitted in the daylight. This physical examination gives an endorsement that the developed O-CDs give off blue light due to the existence of functional groups attached to them. O-CDs emitting blue light at 427 nm when excited at 360 nm using a UV lamp can be further authenticated from the excitation and emission spectra shown in Figure 4b. It is fascinating to note from the spectrum obtained in Figure 4c, that the intensity of the emission spectrum changes with distinct values of excitation from 300–420 nm. The emission intensity values of O-CDs initially escalate for excitation values from 300–360 nm, and later decline upon further increases in excitation from 370–420 nm, with a shift towards a higher wavelength pointing to the right side. Furthermore, the FL emission spectra display a redshift with increasing excitation wavelength, spanning from 300 to 420 nm—which is noticeable in the normalized FL emission spectra shown in Figure 4d. In general, CDs are used as fluorescent probes for multicolor imaging on the grounds of their excitation tunability emission feature. Here, the hydrophilic O-CDs showed a maximum FL around 427 nm with an excitation of 360 nm. The quantum yield of O-CDs was calculated as 20% using Equation (1), with quinine sulfate as reference [37]. The higher value of QY is accounted for by the presence of

quantum confinement of peripheral surface traps present on hydrophilic O-CDs [24]. The diverse sizes of O-CDs and the dispersion of distinct surface states related to the various organic functional groups, i.e., hydroxyl, carboxyl, and oxygen-containing groups on the surface of O-CDs, can be associated with the excitation wavelength-dependent emission feature of O-CDs.

$$\text{The quantum yield (QY)} = \text{QY}_R \frac{I_S A_R (n_S)^2}{I_R A_S (n_R)^2} \quad (1)$$

where, “I” is the measured integrated fluorescent emission intensity, “n” is the refractive index of the solvent, and “A” is the absorbance (intensity). The subscript “R” and “S” refer to the known fluorescent reference and standard for the synthesized sample, respectively.

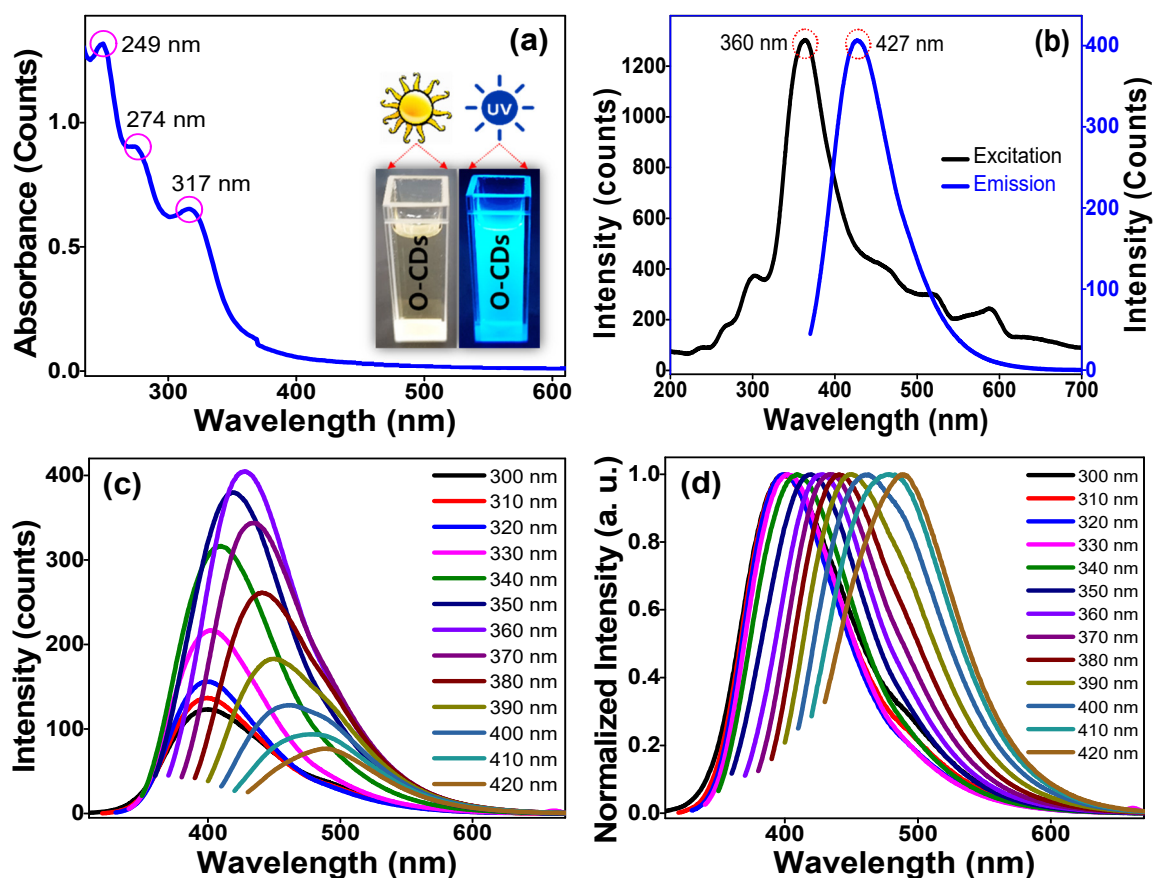


**Figure 4.** (a) UV-visible absorbance spectrum (inset: O-CDs aqueous solution under the illumination of daylight and 365 nm UV light), (b) excitation and emission spectra, (c) excitation-dependent emission spectra, and (d) the corresponding excitation-dependent normalized emission spectra of the synthesized hydrophilic O-CDs.

### 3.2. Stability Studies of the Hydrophilic O-CDs

The photostability of O-CDs is an essential factor towards their implementation in practical applications such as FL chemosensors and bioimaging. For assessing the long-time stability of O-CDs, UV light of 365 nm was shone on O-CDs at different time intervals stored for long periods (1–85 days; Figure 5a). The FL emission spectrum reveals the formation of peaks at the same wavelength (427 nm) position with a slight decline in intensity by increasing the number of days. Additionally, the effects of various UV irradiation times on the FL were studied over the range of 0–75 min, as shown in Figure 5b. Noteworthy, no changes in the spectra with respect to its intensity and wavelength were observed. This observation well confirms the fact that hydrophilic O-CDs have prolonged stability

and photostability against FL photobleaching and are suitable for FL probes for label-free selective and sensitive detection of metal ions.

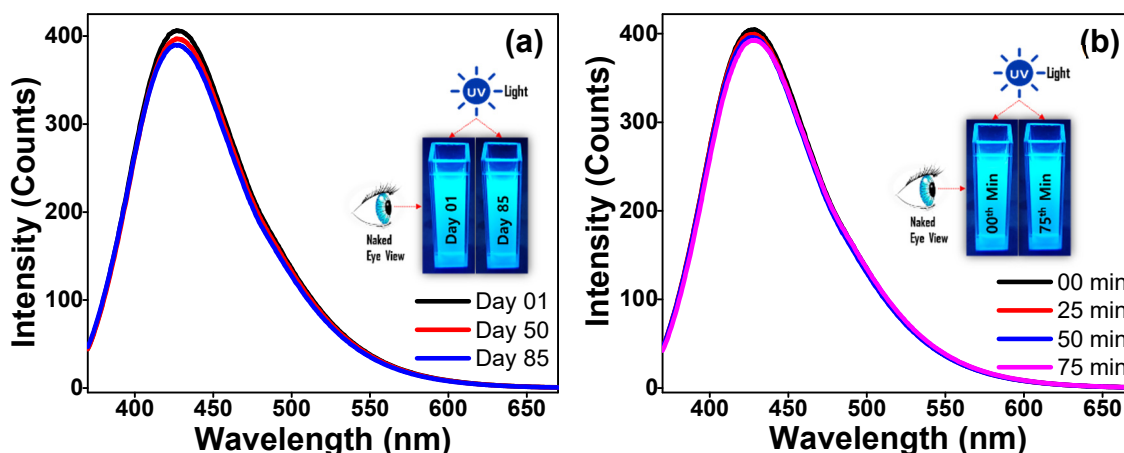


**Figure 5.** (a) Fluorescence emission spectra at different storage times and (b) Fluorescence emission spectra at different irradiation times of the synthesized hydrophilic O-CDs (insets: O-CD aqueous solution under the illumination of 365 nm UV light at different storage time and irradiation time).

### 3.3. Fluorometric Sensing of Metal Ions Using Hydrophilic O-CDs

The presence of various functional groups on hydrophilic O-CDs extracted from *Oxalis corniculata* can be exploited for the sensing of various metal ions, cations, and other toxic elements by accessing the quenching performance. Here these hydrophilic O-CDs were subjected to various ions such as  $\text{Al}^{3+}$ ,  $\text{Ca}^{2+}$ ,  $\text{Cd}^{2+}$ ,  $\text{Co}^{2+}$ ,  $\text{Cr}^{2+}$ ,  $\text{Cu}^{2+}$ ,  $\text{Fe}^{3+}$ ,  $\text{Hg}^{2+}$ ,  $\text{Mn}^{2+}$ ,  $\text{Ni}^{2+}$ ,  $\text{Pb}^{2+}$ , and  $\text{Zn}^{2+}$ , with the concentrations of metal ions at  $1000 \mu\text{M}$  to predict the selective FL quenching of  $\text{Fe}^{3+}$ , as shown in Figure 6a. From the spectrum, it was perceived that the FL emission intensity of  $\text{Fe}^{3+}$  ions decayed drastically, indicating the influence of  $\text{Fe}^{3+}$  ions towards higher quenching effects on the FL behavior of hydrophilic O-CDs compared to other ions. The FL quenching towards various ion selectivities was studied with a bar diagram, as shown in Figure 6b. It was observed that  $\text{Fe}^{3+}$  ions were detected easily by hydrophilic O-CDs can be due to their remarkable affinity among them. Presumably,  $\text{Fe}^{3+}$  formed a complex with functional groups present on hydrophilic O-CDs and resisted the hydrolysis process of  $\text{Fe}^{3+}$  in solution. As a result, the  $\text{Fe}^{3+}$  ions bind to amino and carboxyl groups on the surface of O-CDs, disrupting the radiative transition and causing FL quenching. Furthermore, these findings clearly showed that the O-CD FL sensor was extremely selective for  $\text{Fe}^{3+}$  ion over other metal ions. The FL of aqueous O-CDs in the presence of  $\text{Fe}^{3+}$  ions was examined under normal (daylight) and UV light (365 nm) and shown as the inset of Figure 6b. As shown in inset Figure 6b, the aqueous O-CDs in the presence of  $\text{Fe}^{3+}$  ions displayed a yellow colour under daylight instead of pale yellow, the color of the aqueous O-CDs (inset Figure 4a). However, the aqueous O-CDs in the presence of  $\text{Fe}^{3+}$  ions under UV light did not emit any light because of the quenching of FL. These digital photographs support the quenching effect of O-CDs in the presence of  $\text{Fe}^{3+}$  ions. To study the quenching limit, Figure 6c shows the FL response of the synthesized hydrophilic O-CDs in the presence of ferric ions with different concentrations ranging from 0 to  $50 \mu\text{M}$ . It was observed that with the increase in the concentration of  $\text{Fe}^{3+}$  ions, the intensity of the FL peak quenched gradually with no shift in emission wavelength. Figure 6d shows the relationship between  $(F_0/F)$  and the different concentrations of  $\text{Fe}^{3+}$  ions (0– $50 \mu\text{M}$ ); where  $F_0$  and  $F$  represent FL intensities without and with  $\text{Fe}^{3+}$  ions respectively. The linear graph obtained indicates that  $F_0/F$  is linearly correlated, i.e.,  $R^2 = 0.998$ , with the concentration of  $\text{Fe}^{3+}$  ions. The FL of O-CDs is quenched in the vicinity of  $\text{Fe}^{3+}$  ions due to electron transfer/energy transfer (ET) between the O-CDs and metal ions, which may be used to

identify metal ions effectively. The additional feature of *O*-CDs is that they can both donate and receive electrons. Equation (2) is used to calculate the limit of detection (LOD):

$$\text{LOD} = \frac{3\sigma}{S} \quad (2)$$

where  $\sigma$  is the standard deviation ( $n = 5$ ) and  $S$  is the slope of the linear calibration plot. LOD was calculated as  $0.73 \mu\text{M}$ , demonstrating the sensitivity of hydrophilic *O*-CDs derived from *Oxalis corniculata* in detecting lower levels of  $\text{Fe}^{3+}$  ions in water using the FL quenching method. Table 1 below shows the comparison study of various fluorescent sensors derived from natural sources for the detection of  $\text{Fe}^{3+}$  ions in water. Among various compared reports, our findings exhibited moderate values for the obtained LOD and QY [18,24,33,38,46–53].

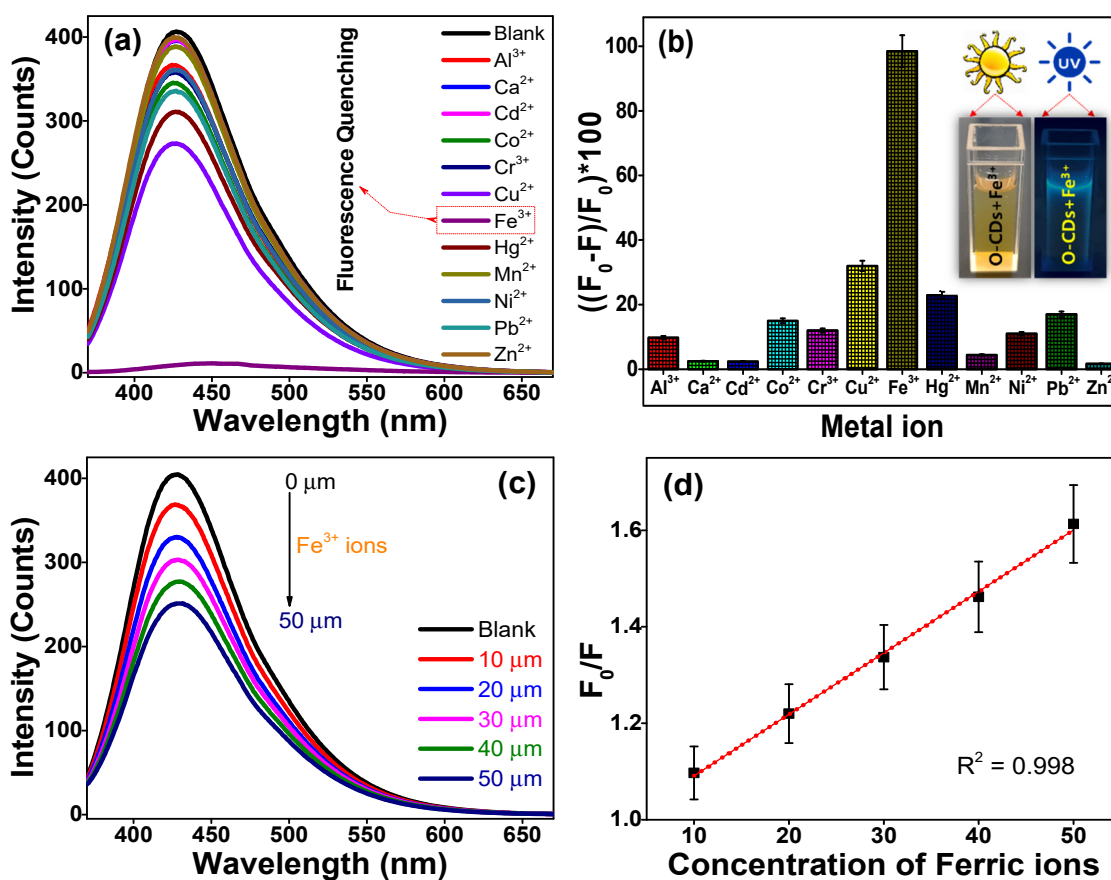


**Figure 6.** (a) Fluorescence response of the synthesized hydrophilic *O*-CDs in the presence of different metal ions (concentrations of metal ions are 1000  $\mu\text{M}$ ) and (b) corresponding relationship between  $((F_0 - F)/F_0) \times 100$  and different metal ions (inset: photograph of *O*-CDs in the presence of  $\text{Fe}^{3+}$  ions under normal (daylight) and UV light (365 nm)). (c) Fluorescence response of the synthesized hydrophilic *O*-CDs in the presence of ferric ions with different concentrations and (d) corresponding relationship between  $(F_0/F)$  and the different concentrations of  $\text{Fe}^{3+}$  ions.

The presence of abundant functional groups such as carboxyl, hydroxyl, and amino groups on the surface or edges of the *O*-CDs is confirmed from the characterization. These functional groups have sensitivity to  $\text{Fe}^{3+}$  ions and make a coordination adduct (*O*-CDs +  $\text{Fe}^{3+}$  complex), which causes the FL quenching of *O*-CDs [54]. A plausible mechanism for the FL quenching is shown in Figure 7. Quenching of *O*-CDs occurs by the intramolecular photoinduced ET process from excited *O*-CDs to  $\text{Fe}^{3+}$  ions. The electron-deficient  $\text{Fe}^{3+}$  complexes with functional groups such as carboxyl, hydroxyl, and amino groups on the surface of *O*-CDs lead to the splitting of the d-orbital of  $\text{Fe}^{3+}$ . The electrons in the

excited state of O-CDs were partially transferred to the d-orbital of  $\text{Fe}^{3+}$ . Thus, the electron transition in the radiation forms (FL emission) is controlled and leads to fluorescence quenching [55].

**Table 1.** Comparison of the different fluorescent sensors from natural sources for the selective sensing of ferric ions in water medium.

No.	Carbon Precursor	Excitation (nm)	QY (%)	LOD/Linear Range ( $\mu\text{M}$ )	Reference
1	Onion waste	380	28	0.31/ 0–20	[46]
2	Rice residue	365	23.48	0.74/3.3–32.2	[47]
3	Sweet potato	360	8.64	0.32/1–100	[48]
4	Black soya bean	360	38.7	0.096/0.2–300	[49]
5	Lychee waste	365	23.5	0.023/0–1.6	[50]
6	Cranberry beans	380	10.85	9.55/30–600	[51]
7	<i>Phyllanthus acidus</i>	350	14	0.9/2–25	[18]
8	<i>Prunus avium</i>	310	13	0.96/0–100	[38]
9	<i>Chionanthus retusus</i>	340	9	70/ 0–25	[24]
10	Diammonium hydrogen citrate	420	46.4	19/0–300	[52]
11	Cellulose fibers	360	32	0.96/25–250	[53]
12	Kiwi fruit peel	360	19	0.85/5–25	[33]
13	<i>Oxalis corniculata</i>	360	20	0.73/10–50	This Work

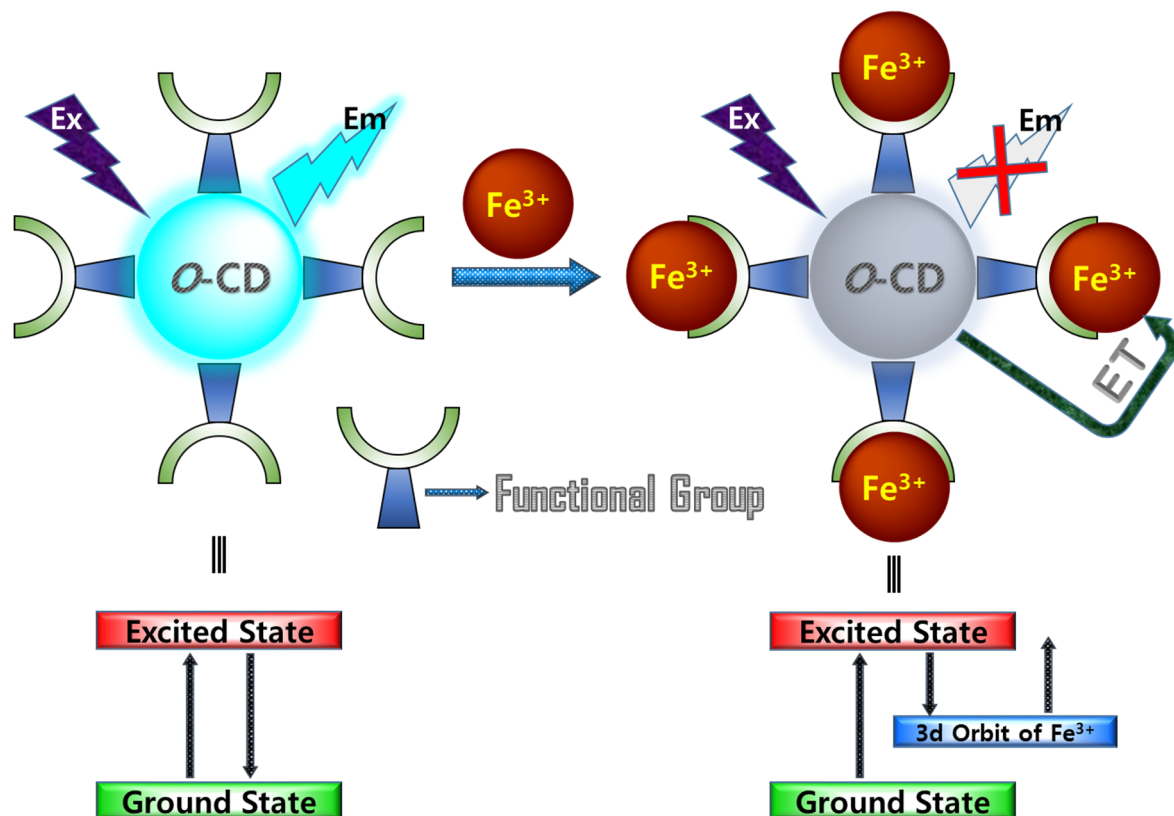


**Figure 7.** Fluorescence quenching mechanism of the O-CDs in the presence of  $\text{Fe}^{3+}$  ions.

#### 4. Conclusions

Using *Oxalis corniculata* extract as a carbon precursor, an environmentally friendly, low-cost, and simple approach for the synthesis of O-CDs was developed. The produced

O-CDs had a near-spherical shape and an adequate degree of graphitization at the core, with an average diameter of 4.5 nm. Raman spectroscopy studies confirmed moderate graphitized O-CD carbon with disordered carbon planes due to surface functional groups. ATR-FTIR and XPS spectroscopy investigations further confirmed the presence of various phytoconstituents, i.e., carbonyl, amine, carboxyl, and hydroxyl groups, along with nitrogen and oxygen-rich molecules of *Oxalis corniculata* found on the surface of O-CDs. The biocompatible O-CDs, when subjected to UV irradiation with an excitation wavelength of 360 nm, produced blue fluorescence at an emission wavelength of 427 nm. Due of their functionality, biomass O-CDs have good water dispersibility/solubility and displayed strong blue FL without further surface modification. The O-CDs showed excellent excitation-emission FL at a range of 300–420 nm, delivering a quantum yield of 20%. The synthesized O-CDs with excitation-emission FL characteristics were utilized as a fluorescent probe to detect Fe<sup>3+</sup> ions in water with high sensitivity and selectivity. Furthermore, the produced O-CDs have a high sensitivity and selectivity for Fe<sup>3+</sup> detection with an LOD of 0.73 μM throughout a concentration range of 10 to 50 μM, suggesting that O-CDs are an efficient chemosensor for Fe<sup>3+</sup> detection. Furthermore, crucially, these findings may inspire the development of cost-effective, environmentally friendly, and long-lasting high-fluorescence multifunctional carbon-based nanomaterials with a variety of future uses, including environmental, biomedical, and optoelectronic applications.

**Supplementary Materials:** The following are available online at <https://www.mdpi.com/article/10.3390/chemosensors9110301/s1>, Materials, Instrumentation methods, quantum yield measurement, photobleaching and prolonging stability measurement, sensing of ferric ion measurement, Figure S1: (a–d) FESEM images with different magnifications of the synthesized hydrophilic O-CDs, Figure S2: (a) XRD pattern and (b) Raman spectrum of the synthesized hydrophilic O-CDs, Figure S3: ATR-FTIR spectrum of the synthesized hydrophilic O-CDs.

**Author Contributions:** Conceptualization, data curation, formal analysis, investigation and writing—original draft, R.A.; Investigation and writing—original draft, S.C.K.; Methodology and resources, T.N.J.I.E.; Writing—review and editing, S.P.; Formal analysis and validation, R.V.; Investigation and visualization, A.K.S.; Investigation and validation, R.S.B.; Visualization, M.A.; Project administration and supervision, Y.R.L. All authors equally contributed to this work. All authors have read and agreed to the published version of the manuscript.

**Funding:** This work was supported by the National Research Foundation of Korea (NRF) grant funded by the Korean government MSIT (2021R1A2B5B02002436).

**Institutional Review Board Statement:** Not applicable.

**Informed Consent Statement:** Not applicable.

**Data Availability Statement:** No data availability.

**Acknowledgments:** Authors thank the National Research Foundation of Korea (NRF) for providing financial support.

**Conflicts of Interest:** The authors declare no conflict of interest.

## References

1. Malik, L.A.; Bashir, A.; Qureashi, A.; Pandith, A.H. Detection and removal of heavy metal ions: A review. *Environ. Chem. Lett.* **2019**, *17*, 1495–1521.
2. Wu, Y.; Pang, H.; Liu, Y.; Wang, X.; Yu, S.; Fu, D.; Chen, J.; Wang, X. Environmental remediation of heavy metal ions by novel-nanomaterials: A review. *Environ. Pollut.* **2019**, *246*, 608–620. [[CrossRef](#)]
3. Han, Y.; Wu, X.; Zhang, X.; Zhou, Z.; Lu, C. Dual functional biocomposites based on polydopamine modified cellulose nanocrystal for Fe<sup>3+</sup>-pollutant detecting and autoblocking. *ACS Sustain. Chem. Eng.* **2016**, *4*, 5667–5673. [[CrossRef](#)]
4. Li, N.; Araya, S.S.; Kær, S.K. The effect of Fe<sup>3+</sup> contamination in feed water on proton exchange membrane electrolyzer performance. *Int. J. Hydrogen Energy* **2019**, *44*, 12952–12957. [[CrossRef](#)]
5. Skalnaya, M.G.; Skalny, A.V. *Essential Trace Elements in Human Health: A Physician's View*; Publishing House of Tomsk State University: Tomsk, Russia, 2018.

6. Saboor, M.; Zehra, A.; Hamali, H.A.; Mobarki, A.A. Revisiting Iron Metabolism, Iron Homeostasis and Iron Deficiency Anemia. *Clin. Lab.* **2021**, *67*.
7. Barić, N.; Cetina, M. Initial bonding of ferric ion ( $\text{Fe}^{3+}$ ) and amyloid beta (A $\beta$ ) peptide as the precondition for oxidative stress in Alzheimer's disease. *Glycative Stress Res.* **2017**, *4*, 250–265.
8. Borase, P.N.; Thale, P.B.; Sahoo, S.K.; Shankarling, G.S. An “off-on” colorimetric chemosensor for selective detection of  $\text{Al}^{3+}$ ,  $\text{Cr}^{3+}$  and  $\text{Fe}^{3+}$ : Its application in molecular logic gate. *Sens. Actuators B: Chem.* **2015**, *215*, 451–458.
9. Kaviani, S.; Izadyar, M.; Housaindokht, M.R. DFT investigation on the selective complexation of  $\text{Fe}^{3+}$  and  $\text{Al}^{3+}$  with hydroxypyridinones used for treatment of the aluminium and iron overload diseases. *J. Mol. Graph. Model.* **2018**, *80*, 182–189. [[PubMed](#)]
10. Van Campenhout, A.; Van Campenhout, C.; Lagrou, A.R.; Manuel-y-Keenoy, B. Effects of in vitro glycation on  $\text{Fe}^{3+}$  binding and  $\text{Fe}^{3+}$  isoforms of transferrin. *Clin. Chem.* **2004**, *50*, 1640–1649.
11. Shahab, U.; Tabrez, S.; Khan, M.S.; Akhter, F.; Khan, M.S.; Saeed, M.; Ahmad, K.; Srivastava, A.; Ahmad, S. Immunogenicity of DNA-advanced glycation end product fashioned through glyoxal and arginine in the presence of  $\text{Fe}^{3+}$ : Its potential role in prompt recognition of diabetes mellitus auto-antibodies. *Chem.-Biol. Interact.* **2014**, *219*, 229–240. [[PubMed](#)]
12. Oh, J.-W.; Kim, T.H.; Yoo, S.W.; Lee, Y.O.; Lee, Y.; Kim, H.; Kim, J.; Kim, J.S. Multisignaling metal sensor: Optical, electrochemical, and electrochemiluminescent responses of cruciform-shaped alkynylpyrene for selective recognition of  $\text{Fe}^{3+}$ . *Sens. Actuators B Chem.* **2013**, *177*, 813–817.
13. Sayed, A.; Othman, I.M.; Hamam, M.; Gomaa, H.; Gadallah, M.I.; Mostfa, M.; Ali, H.R.H.; Emran, M.Y.; Abdel-Hakim, M.; Mahross, M. A novel fluorescent sensor for fast and highly selective turn-off detection of  $\text{Fe}^{3+}$  in water and pharmaceutical samples using synthesized azopyrazole-benzenesulfonamide derivative. *J. Mol. Struct.* **2021**, *1225*, 129175. [[CrossRef](#)]
14. Wang, S.; Du, L.; Zhang, A.; Li, B. Catalytic kinetic determination of trace amounts of iron (III) with polarographic detection. *Anal. Lett.* **1997**, *30*, 2099–2107.
15. Bakkaus, E.; Collins, R.N.; Morel, J.-L.; Gouget, B. Anion exchange liquid chromatography–inductively coupled plasma-mass spectrometry detection of the  $\text{Co}^{2+}$ ,  $\text{Cu}^{2+}$ ,  $\text{Fe}^{3+}$  and  $\text{Ni}^{2+}$  complexes of mugineic and deoxymugineic acid. *J. Chromatogr. A* **2006**, *1129*, 208–215. [[CrossRef](#)] [[PubMed](#)]
16. Johnson, A.D.; Curtis, R.M.; Wallace, K.J. Low molecular weight fluorescent probes (LMFPs) to detect the group 12 metal triad. *Chemosensors* **2019**, *7*, 22. [[CrossRef](#)]
17. Fares, N.V.; Medhat, P.M.; El Maraghy, C.M.; Okeil, S.; Ayad, M.F. Influence of Nitrogen-Doped Carbon Dot and Silver Nanoparticle Modified Carbon Paste Electrodes on the Potentiometric Determination of Tobramycin Sulfate: A Comparative Study. *Chemosensors* **2021**, *9*, 52.
18. Atchudan, R.; Edison, T.N.J.I.; Aseer, K.R.; Perumal, S.; Karthik, N.; Lee, Y.R. Highly fluorescent nitrogen-doped carbon dots derived from *Phyllanthus acidus* utilized as a fluorescent probe for label-free selective detection of  $\text{Fe}^{3+}$  ions, live cell imaging and fluorescent ink. *Biosens. Bioelectron.* **2018**, *99*, 303–311. [[CrossRef](#)]
19. Singh, P.; Mittal, L.S.; Vanita, V.; Kumar, K.; Walia, A.; Bhargava, G.; Kumar, S. Self-assembled vesicle and rod-like aggregates of functionalized perylene diimide: Reaction-based near-IR intracellular fluorescent probe for selective detection of palladium. *J. Mater. Chem. B* **2016**, *4*, 3750–3759. [[CrossRef](#)]
20. Pramanik, B.; Ahmed, S.; Singha, N.; Das, D. Self-Assembly Assisted Tandem Sensing of  $\text{Pd}^{2+}$  and  $\text{CN}^-$  by a Perylenediimide-Peptide Conjugate. *ChemistrySelect* **2017**, *2*, 10061–10066. [[CrossRef](#)]
21. Yuan, L.; Lin, W.; Zheng, K.; He, L.; Huang, W. Far-red to near infrared analyte-responsive fluorescent probes based on organic fluorophore platforms for fluorescence imaging. *Chem. Soc. Rev.* **2013**, *42*, 622–661.
22. Wei, X.; Li, H.; Li, Z.; Vuki, M.; Fan, Y.; Zhong, W.; Xu, D. Metal-enhanced fluorescent probes based on silver nanoparticles and its application in IgE detection. *Anal. Bioanal. Chem.* **2012**, *402*, 1057–1063. [[PubMed](#)]
23. Rizvi, S.B.; Ghaderi, S.; Keshtgar, M.; Seifalian, A.M. Semiconductor quantum dots as fluorescent probes for in vitro and in vivo bio-molecular and cellular imaging. *Nano Rev.* **2010**, *1*, 5161.
24. Atchudan, R.; Edison, T.N.J.I.; Chakradhar, D.; Perumal, S.; Shim, J.-J.; Lee, Y.R. Facile green synthesis of nitrogen-doped carbon dots using *Chionanthus retusus* fruit extract and investigation of their suitability for metal ion sensing and biological applications. *Sens. Actuators B Chem.* **2017**, *246*, 497–509.
25. Atchudan, R.; Edison, T.N.J.I.; Aseer, K.R.; Perumal, S.; Lee, Y.R. Hydrothermal conversion of *Magnolia liliiflora* into nitrogen-doped carbon dots as an effective turn-off fluorescence sensing, multi-colour cell imaging and fluorescent ink. *Colloids Surf. B Biointerfaces* **2018**, *169*, 321–328. [[CrossRef](#)] [[PubMed](#)]
26. Cali, F.; Cantaro, V.; Fichera, L.; Ruffino, R.; Trusso Sfrazzetto, G.; Li-Destri, G.; Tuccitto, N. Carbon Quantum Dots from Lemon Waste Enable Communication among Biodevices. *Chemosensors* **2021**, *9*, 202. [[CrossRef](#)]
27. LeCroy, G.E.; Sonkar, S.K.; Yang, F.; Veca, L.M.; Wang, P.; Tackett, K.N.; Yu, J.-J.; Vasile, E.; Qian, H.; Liu, Y.; et al. Toward Structurally Defined Carbon Dots as Ultracompact Fluorescent Probes. *ACS Nano* **2014**, *8*, 4522–4529. [[CrossRef](#)]
28. Lee, H.; Su, Y.-C.; Tang, H.-H.; Lee, Y.-S.; Lee, J.-Y.; Hu, C.-C.; Chiu, T.-C. One-Pot Hydrothermal Synthesis of Carbon Dots as Fluorescent Probes for the Determination of Mercuric and Hypochlorite Ions. *Nanomaterials* **2021**, *11*, 1831.
29. Xie, Y.; Cheng, D.; Liu, X.; Han, A. Green Hydrothermal Synthesis of N-doped Carbon Dots from Biomass Highland Barley for the Detection of  $\text{Hg}^{2+}$ . *Sensors* **2019**, *19*, 3169. [[CrossRef](#)]

30. Pu, Z.-F.; Wen, Q.-L.; Yang, Y.-J.; Cui, X.-M.; Ling, J.; Liu, P.; Cao, Q.-E. Fluorescent carbon quantum dots synthesized using phenylalanine and citric acid for selective detection of Fe<sup>3+</sup> ions. *Spectrochim. Acta Part A Mol. Biomol. Spectrosc.* **2020**, *229*, 117944. [[CrossRef](#)]
31. Zu, F.; Yan, F.; Bai, Z.; Xu, J.; Wang, Y.; Huang, Y.; Zhou, X. The quenching of the fluorescence of carbon dots: A review on mechanisms and applications. *Microchim. Acta* **2017**, *184*, 1899–1914. [[CrossRef](#)]
32. Jorns, M.; Pappas, D. A Review of Fluorescent Carbon Dots, Their Synthesis, Physical and Chemical Characteristics, and Applications. *Nanomaterials* **2021**, *11*, 1448. [[PubMed](#)]
33. Atchudan, R.; Edison, T.N.J.I.; Perumal, S.; Vinodh, R.; Sundramoorthy, A.K.; Babu, R.S.; Lee, Y.R. Leftover Kiwi Fruit Peel-Derived Carbon Dots as a Highly Selective Fluorescent Sensor for Detection of Ferric Ion. *Chemosensors* **2021**, *9*, 166.
34. Iravani, S.; Varma, R.S. Green synthesis, biomedical and biotechnological applications of carbon and graphene quantum dots. A review. *Environ. Chem. Lett.* **2020**, *18*, 703–727.
35. Kang, C.; Huang, Y.; Yang, H.; Yan, X.F.; Chen, Z.P. A review of carbon dots produced from biomass wastes. *Nanomaterials* **2020**, *10*, 2316.
36. Li, F.; Yang, D.; Xu, H. Non-Metal-Heteroatom-Doped Carbon Dots: Synthesis and Properties. *Chem.—A Eur. J.* **2019**, *25*, 1165–1176. [[CrossRef](#)]
37. Atchudan, R.; Edison, T.N.J.I.; Perumal, S.; Muthuchamy, N.; Lee, Y.R. Hydrophilic nitrogen-doped carbon dots from biowaste using dwarf banana peel for environmental and biological applications. *Fuel* **2020**, *275*, 117821. [[CrossRef](#)]
38. Edison, T.N.J.I.; Atchudan, R.; Shim, J.-J.; Kalimuthu, S.; Ahn, B.-C.; Lee, Y.R. Turn-off fluorescence sensor for the detection of ferric ion in water using green synthesized N-doped carbon dots and its bio-imaging. *J. Photochem. Photobiol. B Biol.* **2016**, *158*, 235–242.
39. Atchudan, R.; Edison, T.N.J.I.; Perumal, S.; Vinodh, R.; Lee, Y.R. Betel-derived nitrogen-doped multicolor carbon dots for environmental and biological applications. *J. Mol. Liq.* **2019**, *296*, 111817.
40. Atchudan, R.; Edison, T.N.J.I.; Lee, Y.R. Nitrogen-doped carbon dots originating from unripe peach for fluorescent bioimaging and electrocatalytic oxygen reduction reaction. *J. Colloid Interface Sci.* **2016**, *482*, 8–18.
41. Kiran, K.; Awathade, K.; Kumar, J.; Kanthesh, B. Protective Effect of Oxalis Corniculate Extract against Toxic Enzymes of Najanaja and Daboiarusselli Venom. *Ann. Rom. Soc. Cell Biol.* **2021**, *25*, 7304–7316.
42. Wei, W.; Huang, J.; Gao, W.; Lu, X.; Shi, X. Carbon Dots Fluorescence-Based Colorimetric Sensor for Sensitive Detection of Aluminum Ions with a Smartphone. *Chemosensors* **2021**, *9*, 25.
43. Hsu, P.-C.; Shih, Z.-Y.; Lee, C.-H.; Chang, H.-T. Synthesis and analytical applications of photoluminescent carbon nanodots. *Green Chem.* **2012**, *14*, 917–920. [[CrossRef](#)]
44. Boukaoud, A.; Chiba, Y.; Sebbar, D. A periodic DFT study of IR spectra of amino acids: An approach toward a better understanding of the NH and OH stretching regions. *Vib. Spectrosc.* **2021**, *116*, 103280. [[CrossRef](#)]
45. Zhao, Z.; Yang, Z.; Hu, Y.; Li, J.; Fan, X. Multiple functionalization of multi-walled carbon nanotubes with carboxyl and amino groups. *Appl. Surf. Sci.* **2013**, *276*, 476–481. [[CrossRef](#)]
46. Bandi, R.; Gangapuram, B.R.; Dadigala, R.; Eslavath, R.; Singh, S.S.; Guttena, V. Facile and green synthesis of fluorescent carbon dots from onion waste and their potential applications as sensor and multicolour imaging agents. *RSC Adv.* **2016**, *6*, 28633–28639. [[CrossRef](#)]
47. Qi, H.; Teng, M.; Liu, M.; Liu, S.; Li, J.; Yu, H.; Teng, C.; Huang, Z.; Liu, H.; Shao, Q.; et al. Biomass-derived nitrogen-doped carbon quantum dots: Highly selective fluorescent probe for detecting Fe<sup>3+</sup> ions and tetracyclines. *J. Colloid Interface Sci.* **2019**, *539*, 332–341. [[CrossRef](#)]
48. Shen, J.; Shang, S.; Chen, X.; Wang, D.; Cai, Y. Facile synthesis of fluorescence carbon dots from sweet potato for Fe(3+) sensing and cell imaging. *Mater. Sci. Eng. C Mater. Biol. Appl.* **2017**, *76*, 856–864. [[CrossRef](#)]
49. Jia, J.; Lin, B.; Gao, Y.; Jiao, Y.; Li, L.; Dong, C.; Shuang, S. Highly luminescent N-doped carbon dots from black soya beans for free radical scavenging, Fe<sup>3+</sup> sensing and cellular imaging. *Spectrochim. Acta Part A Mol. Biomol. Spectrosc.* **2019**, *211*, 363–372. [[CrossRef](#)]
50. Sahoo, N.K.; Jana, G.C.; Aktara, M.N.; Das, S.; Nayim, S.; Patra, A.; Bhattacharjee, P.; Bhadra, K.; Hossain, M. Carbon dots derived from lychee waste: Application for Fe(3+) ions sensing in real water and multicolor cell imaging of skin melanoma cells. *Mater. Sci. Eng. C Mater. Biol. Appl.* **2020**, *108*, 110429. [[CrossRef](#)]
51. Zulfajri, M.; Gedda, G.; Chang, C.-J.; Chang, Y.-P.; Huang, G.G. Cranberry Beans Derived Carbon Dots as a Potential Fluorescence Sensor for Selective Detection of Fe<sup>3+</sup> Ions in Aqueous Solution. *ACS Omega* **2019**, *4*, 15382–15392. [[CrossRef](#)]
52. Khan, W.U.; Wang, D.; Zhang, W.; Tang, Z.; Ma, X.; Ding, X.; Du, S.; Wang, Y. High quantum yield green-emitting carbon dots for Fe (III) detection, biocompatible fluorescent ink and cellular imaging. *Sci. Rep.* **2017**, *7*, 1–9.
53. Yang, G.; Wan, X.; Su, Y.; Zeng, X.; Tang, J. Acidophilic S-doped carbon quantum dots derived from cellulose fibers and their fluorescence sensing performance for metal ions in an extremely strong acid environment. *J. Mater. Chem. A* **2016**, *4*, 12841–12849. [[CrossRef](#)]
54. Zhou, X.; Zhao, G.; Tan, X.; Qian, X.; Zhang, T.; Gui, J.; Yang, L.; Xie, X. Nitrogen-doped carbon dots with high quantum yield for colorimetric and fluorometric detection of ferric ions and in a fluorescent ink. *Microchim. Acta* **2019**, *186*, 67. [[CrossRef](#)] [[PubMed](#)]
55. Zhao, L.; Wang, Y.; Zhao, X.; Deng, Y.; Xia, Y. Facile Synthesis of Nitrogen-Doped Carbon Quantum Dots with Chitosan for Fluorescent Detection of Fe<sup>3+</sup>. *Polymers* **2019**, *11*, 1731. [[CrossRef](#)]